# Highlights

**From Soil to Printed Structures: A Systematic Approach to Designing Clay-Based Materials for 3D Printing in Construction and Architecture**

Ofer Asaf, Arnon Bentur, Pavel Larianovsky, Aaron Sprecher

- Flow-table and rigidity test evaluates mixture performance in green state.
- Clay particle grading and composition affect the rheological properties and printing performance.
- Analytical model predicts stability and failure of 3D printed soil elements.
- Disparity between green and hardened states of clay mixes in 3D printing is identified.

# From Soil to Printed Structures: A Systematic Approach to Designing Clay-Based Materials for 3D Printing in Construction and Architecture

Ofer Asaf[a], Arnon Bentur[b], Pavel Larianovsky[b], Aaron Sprecher[a]

[a] *Faculty of Architecture and Town Planning, Technion - Israel Institute of Technology, Haifa, 3200003, Israel*
[b] *Faculty of Civil and Environmental Engineering, Technion - Israel Institute of Technology, Haifa, 3200003, Israel*

## Abstract

Three-dimensional (3D) printing of clayey soils has gained traction in construction and architecture due to its eco-friendliness and design advantages. However, no comprehensive method is yet available for transforming these soils into a mix that flows and is stable. To develop such a method, we measured the rheological properties and tested the performance of 12 mixtures of sand and clay using rigidity and pumping tests and then compared the linear relationships between the various results. This was followed by an *in situ* printing test. An analytical model for predicting the plastic collapse of the bottom layer was used. To better elucidate the failure mechanism, we correlated digital images of the mixtures. Finally, the mechanical properties of the mixtures were assessed at 14 and 28 days. The research indicates that results from flow-table tests and custom rigidity tests optimize mixtures for 3D printing. Rheological findings show that increased kaolinite enhances the thixotropicity of the mix. Coarser particles improve the static yield because of elevated interparticle friction. *In situ* printing tests suggest that a rotational rheometer test can predict element failure from plastic collapse based on the printing parameters. Finally, the mechanical properties differ between fresh and hardened clay-soil mixtures.

*Keywords:* 3D printing, Soil-based materials, Buildability, Robotic fabrication, Earth construction

## 1. Introduction

Additive manufacturing (often referred to as three-dimensional or “3D” printing) using clayey soils has gained interest in the architectural and construction sector [1, 2, 3, 4], driven by several prominent factors. First, 3D printing technologies, noted for their capacity to produce advanced designs, allow architects and engineers to design optimized and innovative structures [5, 6]. Second, escalating environmental concerns in the construction sector has catalyzed a search for sustainable materials [7]. In this context, soils have emerged as an alternative to traditional construction materials because of their reduced environmental footprint [8, 9] and their adaptability within a circular economy framework [10, 11].

The synergy between 3D printing and using soils as construction materials presents extensive application opportunities, ranging from small-scale elements to large-scale structures. Examples of these structures include integrated wall components [12], elements designed for green infrastructure [13], structures geared toward low-impact affordable housing [14], and architectural edifices [15]. Moreover, 3D printing of soils also captures interest for extraterrestrial construction [16, 17]. In these scenarios, local regolith, rich in amorphous inorganic compounds, promises potential transformation by alkalis into geopolymer binders [18]. All these applications underscore the need for clear guidelines to convert local soils into 3D-printable mixtures [19].

Understanding the rheological properties of such materials is essential to using them in designs [20, 21]. These properties govern the material's transportation through the pumping system and determine the layer stability post-deposition [22]. A 3D printable material should be endowed with two contrasting and balanced characteristics: (i) the ability to flow through the pumping system and (ii) rigidity upon deposition. Initiating material flow requires surpassing the critical shear stress (delineated as the static yield stress $\tau_{0s}$). Next, the mixture enters a dynamic state where the shear strain rate becomes linear in shear stress, as described by the Bingham model [23]. The parameters of this model can be expressed in terms of yield stress and apparent viscosity $\mu$, where the intersection of this linear relationship with the shear axis at zero shear strain rate is the dynamic yield stress $\tau_{0d}$ of the material [24].

When a material is conveyed to the printhead for material processing, a phenomenon known as "plug flow" occurs due to the material's heightened viscosity [25]. This flow state results in pressure loss, primarily due to particle friction against the delivery hose. This friction subsequently slows the flow rate, which requires the pump to provide more energy. According to the Bingham model, the pressure loss of materials flowing through a conduit is determined by two factors: yield stress and viscosity. This relationship can be described by the Buckingham–Reiner model [26]. Ideally, to ensure a smooth and efficient flow, a mixture should have both a low dynamic yield stress and low viscosity. Yet, after being extruded from the nozzle, to remain stable, the static yield stress of the material must be quickly elevated. The difference in behavior between these static and dynamic properties is an expression of the material's thixotropy. Consequently, the thixotropic behavior of an optimal 3D printing material should increase rapidly without a corresponding increase in its dynamic properties. While cement-based systems are often thixotropic [27, 28], such behavior is less common with printable clay-based mixtures [29].

The rheological properties of cementitious systems destined for 3D printing have already been discussed in detail. For instance, Roussel introduced a theoretical rheology-based model of printable concrete [30]. This model aims to prevent critical strain, which could collapse the printed bottom layer. Kruger et al. proposed an analytical model grounded in rheological testing to ascertain layer stability during printing [31, 32]. Their model leverages static yield stress and a correction factor tied to the layer's cross section. The model predicts, with a commendable level of accuracy, the potential failure of a printed artifact when its self-weight surpasses the static yield. Furthermore, Kruger applied this model to determine the optimal printing parameters [33]. In the context of earth-based materials, Perrot et al. used a similar method to evaluate the suitability for building of a soil-based mixture, although they did not conduct *in situ* 3D printing tests [29].

Previous publications in the field of 3D printing of soils have sought to design optimal soil-based mixtures. Several methods have been proposed to endow these mixtures with the rheological properties essential for 3D printing. Perrot et al. used an alginate biopolymer to induce a thixotropic effect in earth-based mixtures and analyzed the mix based on a penetrometer test [29]. Biggerstaff et al. used a rotational rheometer to estimate the yield stress of biopolymer bound soil mixtures [34, 35]. Bajpayee et al. presented a holistic approach to 3D soil printing comprising particle distribution, mineralogical composition, and rotational rheometry for inducing a geopolymerization reaction [36]. Silva et al. turned to a shear-vane test and a custom stability test to evaluate the fresh state properties of the mix [37]. Alqenaee et al. explored the various aspects of mixture design by using a deformation test introduced by Bai et al. [38], [39]. In a different vein, Ferreti et al. used rice husk and hydraulic lime to enhance the material's hardened properties

[40]. Faleschini incorporated lime, cement, and vegetable fiber to optimize both the mechanical and economic properties of the soil mixture [41]. Nevertheless, a comprehensive method that unifies basic tests with *in situ* printing evaluations tailored for designing 3D printable clayey soils remains absent. Thus, the short-term rheological characteristics of clay-based materials, crucial for predicting construction speeds [30], have yet to be thoroughly examined. Furthermore, despite their heterogeneous nature, how mineralogical and physical variations affect the 3D printing of local soils remains largely unexplored [42, 43, 44].

Consequently, fundamental guidelines are required for designing and evaluating soil-based mixtures for 3D printing, and these guidelines should reflect the combined characteristics of the soils. Such guidelines could serve as a foundational reference for designing and developing these materials. The primary contribution of this study is to create a shared framework for developing soil-based mixtures and determine the correct printing parameters for 3D printing applications in construction. By considering both material progression and the printing parameters, this research lays the groundwork for refining 3D soil printing.

Multiple mixtures were developed with different particle grading and water content. These were assessed using simple testing methods, rotational rheological tests, and performance results. Linear correlations emerge between the various testing methods and performance results, providing guidelines to find the best performance window for any specified printing equipment. Three different clay types were then tested to gauge the influence of mineralogical and particle grading on the printing behavior. *In situ* cylinder printing was used to predict the collapse of the layer buildup based on rheological properties. Finally, the study explores how clay type affects the mechanical properties of the clays, suggesting a tension between optimizing the green and hardened properties of the mixture.

## 2. Materials and methods

Figure 1 describes the step-by-step experimental method followed in this study.

## 2.1. Materials

The tested mixtures contained quartz dune sand and three types of powdered clay. Sand was sourced from Kfar Giladi Minerals and sieved through a 1.18 mm sieve. White kaolinite clay (white) was procured from Alco Chemicals; brown-red kaolinite clay (chocolate) and yellow marl clay (Mamshit) were obtained from Yehu Clays, Ltd.

## 2.2. X-ray diffraction analysis

A McCrone micronizing device with 16 agate was used to wet-grind the clays. For each preparation, 6 g of each sample and 15 ml of isopropanol were added as grinding media. The samples were ground at 1500 rpm for 15 minutes. After milling, the clays were filtered through a Whatman grade-3 filter paper (6 $\mu$m pore size) using a vacuum pump, rinsed with diethyl ether, and dried for 15 min at 40 °C in a vacuum oven at a 300 mbar of constant pressure. X-ray powder diffraction using a PANalytical EMPYREAN X-ray diffractometer equipped with a Cu-K$\alpha$1,2 radiation tube ($\lambda$ = 1.5408 Å). The x-ray diffraction optical configuration for the incident beam consisted of a 10 mm mask, a 0.04 rad Soller slit, and 1/16 °C divergence and 1/8 °C antiscatter fixed slits. The diffracted-beam optics consisted of a 7.5 mm antiscatter fixed slit and a 0.04 rad Soller slit. The x-ray diffraction data were collected using a 45 kV accelerating voltage and 40 mA current in a conventional Bragg-Brentano $\theta$-2$\theta$ geometry. Data were acquired by scanning samples with a PIXcel 3D detector. All scans were acquired in continuous scan mode over an angular range of 5° to 70° with 0.017° step size for approximately 20 minutes per scan. For Kaoline (18-2023), the range was 3° to 75° (2$\theta$) with the same step of 0.017° 2$\theta$. Quantitative phase analysis was performed by the Rietveld refinement method as implemented in the HighScore Plus software

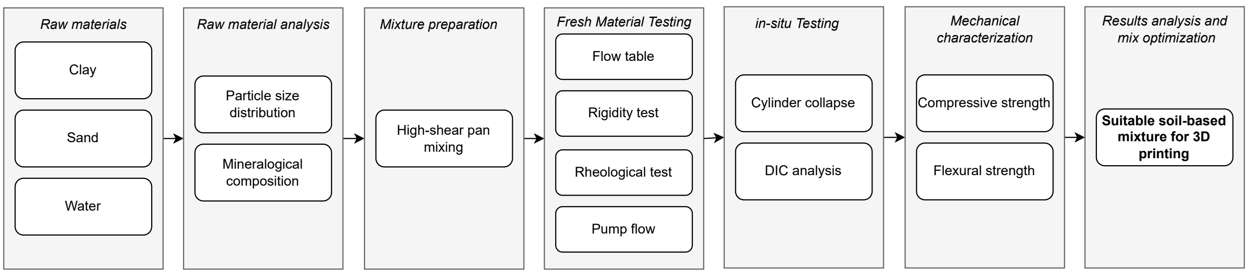


Figure 1: Flow chart illustrating the step-by-step experimental method used in the study.

(Malvern Panalytical). Table 1 presents the results of the mineralogical characterization.

Table 1: Mineralogical composition of raw powdered clay mixtures.

| **Phase** | **Kaolinite** | **Quartz** | **Calcite** | **Illite** | **Muscovite** | **Ivsite** | **Picromerite** | **Orthoclase** |
|---|---|---|---|---|---|---|---|---|
| Sand | 0 | 99.9 | 0.1 | 0 | 0 | 0 | 0 | 0 |
| White | 99.4 | 0.4 | 0 | 0 | 0.2 | 0 | 0 | 0 |
| Chocolate | 76.8 | 12.7 | 1.4 | 0 | 0 | 3.9 | 3.1 | 2.1 |
| Mamshit | 41.5 | 17.0 | 22.9 | 7.0 | 5.0 | 0 | 0 | 6.2 |

### *2.3. Particle size distribution*

A laser diffractometer Mastersizer 3000 Particle Size Analyzer (Malvern Panalytical) was used to analyze the particle-size distribution. A sample of 0.1 g was mixed with 10 ml of isopropanol, followed by 30 s of sonication to avoid aggregation. The mixture was slowly added to the Hydro LV device. Figure 2 shows the particle-size distribution of the raw materials used in this study.

### *2.4. Mixture preparation*

The mixtures were prepared with a high-shear pan mixer. The mixer tank was first filled with all dry ingredients, after which the water was added. Table 2 describes in detail the clay/sand and clay/water ratios of the mixture. Following the addition of water, the materials were mixed intensively for 3 minutes. The mixer was inspected to ensure that no dry ingredients were left unmixed before high-shear mixing for another 6 minutes.

### *2.5. Methods to test green material*

The methods of testing the fresh green material included methods to provide the basic physical and mechanical parameters of the material for 3D printing and standard tests for comparison and characterization.

Flow tests were conducted using the ASTM C230 flow table test for hydraulic cement [45] [see Figure 3(a)]. A brass conical mold was placed at the table center and filled with the mixture. The mold was then removed, the table jolted 25 times, and the spread of the material recorded.

Table 2: Composition of tested white clay-sand mixtures.

| Mix | Clay (wt.%) | Sand (wt.%) | Water (wt.%) |
|---|---|---|---|
| M1 | 19.4 | 65.5 | 15.1 |
| M2 | 21.6 | 62.4 | 16.0 |
| M3 | 24.0 | 60.0 | 16.0 |
| M4 | 23.4 | 58.6 | 18.0 |
| M5 | 24.0 | 59.7 | 16.3 |
| M6 | 24.2 | 60.4 | 15.3 |
| M7 | 24.0 | 60.1 | 15.9 |
| M8 | 28.3 | 54.1 | 17.6 |
| M9 | 28.6 | 54.6 | 16.8 |
| M10 | 30.4 | 51.4 | 18.2 |
| M11 | 33.0 | 49.4 | 17.6 |
| M12 | 32.7 | 49.1 | 18.2 |

The rigidity of the fresh green mixture was characterized as per Kazemian et al. [46] by using the loading apparatus shown in Figure 3(b). The test was done using a cylindrical 185-mm-diameter, 100-mm-high mold. The mold was first filled in two stages with fresh material to ensure proper packing, followed by removal of the mold. A transparent board was placed on top of the material and loaded in increments of 500 g up to an equivalent of 0.18 kPa. The deformation at the four corners of the board was measured and the average deformation was recorded. The test continued up to a load of 2.9 kPa and produced load-deformation curves from which the rigidity coefficient, defined as the slope of the curve, was calculated.

A rheological test was carried out using a commercialized rotational rheometer, ICAR Plus (Germann Instruments Inc.), as shown in Figure 3(c). The geometry of the rheometer consists of a four-bladed vane at the center of a cylindrical container. The test was done in two modes: a stress growth test to determine the static yield strength, and a flow curve test to determine the dynamic yield strength and apparent viscosity.

In the stress growth test, the vane rotation was set to a constant 0.16 rad/s, and the static yield stress was computed by using

$$\tau_{0s} = \frac{2T}{\pi D^3 \left(\frac{H}{D} + \frac{1}{3}\right)}, \tag{1}$$

where $\tau_{0s}$ is the static yield stress, $T$ is the maximum torque recorded, $D$ is the vane diameter, and $H$ is the vane height.

In the flow curve test, rotation rates from 0.31 to 3.14 rad/s were applied to subject the mixture to various shear strains. This led to a linear stress shear-strain rate or rotation-rate curve that may be described by the Bingham model:

$$\tau = \tau_{0d} + \mu\dot{\gamma}, \tag{2}$$

where $\tau_{0d}$ is the dynamic yield stress, $\mu$ is the plastic viscosity, and $\dot{\gamma}$ is the shear strain rate. For all mixtures analyzed, an $R^2$ value of no less than 0.95 was obtained, pointing to a pronounced linear correlation between shear stress and shear strain. Thus, the flow curve gives the two dynamic rheological parameters: dynamic yield stress and apparent coefficient of viscosity.

The above-mentioned rheological measurements were conducted at specific time intervals (0, 0.5, 1, 2, 5, 10, 15, 30, 45 min), with the material remaining stationary in the rheometer during the intervals. This resting period allowed physical bonds to develop between particles and simulated the time elapsed following material deposition from the nozzle in 3D printing.

To evaluate the ability to transport the material through the delivery system, the flow rate of the pump (Figure 4) was recorded at a set voltage of 5 V supplied to the pump control unit.

### *2.6. Statistical analysis for linear correlation*

A statistical analysis was conducted using the NumPy and Matplotlib Python libraries to evaluate linear correlations between the composition, rheological characteristics, and performance parameters of the mixtures. The strength and direction of these linear relationships were quantified by calculating Pearson's correlation coefficient $r$, as described by

$$r = \frac{\sum(x_i - \bar{x})(y_i - \bar{y})}{\sqrt{\sum(x_i - \bar{x})^2 \sum(y_i - \bar{y})^2}}, \tag{3}$$

where $x_i$ and $y_i$ are individual data points and $\bar{x}$ ($\bar{y}$) is the mean of the $x$ ($y$) values. This coefficient ranges between $-1$ and 1 and indicates linearity between two datasets [47]. The aim of the analysis

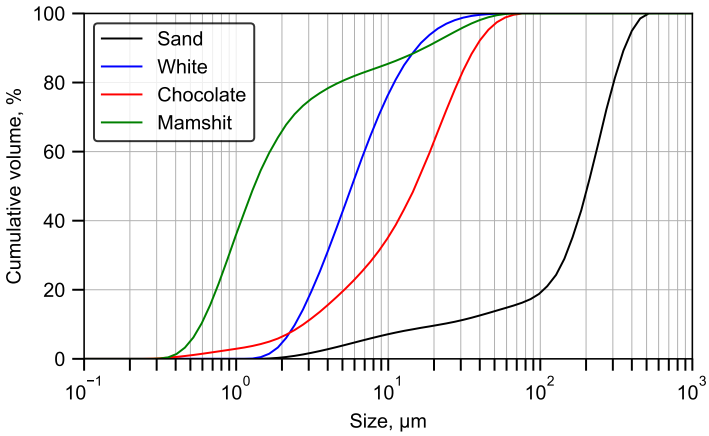


Figure 2: Particle size distribution of raw materials.

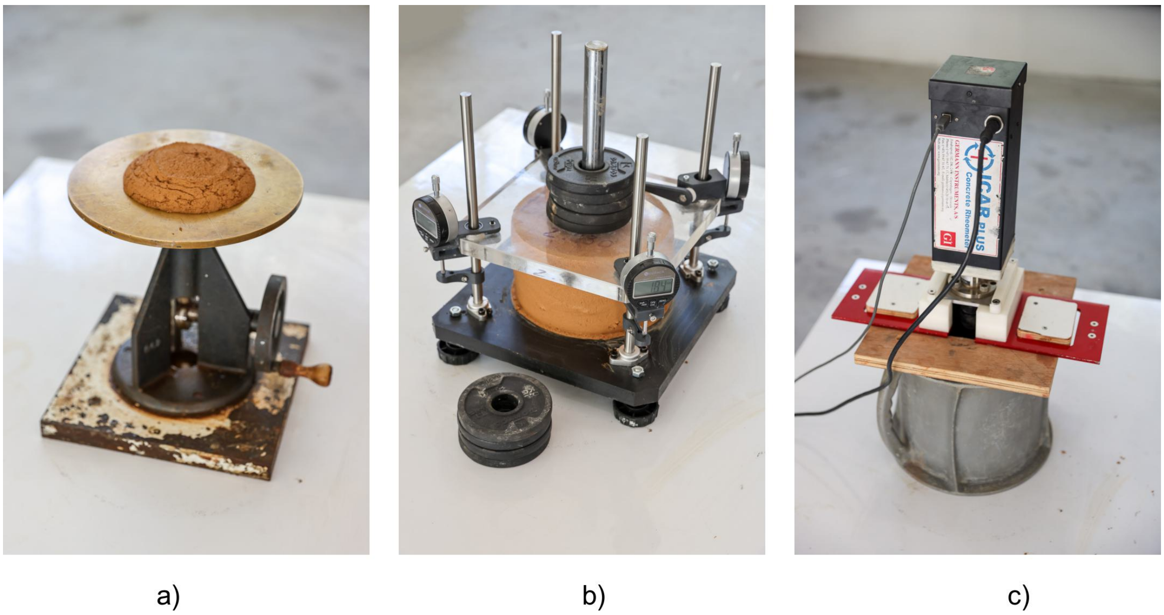


Figure 3: Green material test methods: (a) Flow table test, assessing flow properties through the spread of the mixture after jolting. (b) Fresh green material loading rig for measuring rigidity via deformation under incremental loading. (c) ICAR rheometer for evaluating static and dynamic rheological properties of the mixture.

is to identify potential patterns and dependencies, shedding light on how the mixture's composition and rheological characteristics influence its performance parameters.

### 2.7. *In situ testing*

*In situ* testing involves printing cylindrical samples with a diameter of 180 mm. To continuously monitor the layer heights during the printing process, we recorded video at 30 frames per second. A Canon 6D camera, equipped with a Canon EF 70-200/2.8L IS II lens, was positioned to capture detailed footage of each layer as the printing progressed. This allowed us to closely inspect the print layers throughout the procedure. The experiment continued until the cylinder collapsed, at which point the time to failure and the number of layers at failure were recorded. The printing process was analyzed with digital-image correlation software (Tema PRO by ImageSystems) to evaluate the deformation of the lower layers during printing.

### 2.8. *Mechanical characterization*

For mechanical characterization, specimens from each mixture were prepared in accordance with standards EN 12350-1 for compressive strength and EN 12390-5 for flexural strength. The dimensions of the test specimens were $50 \times 50 \times 50$ mm$^3$ for the compressive strength test and $40 \times 40 \times 160$ mm$^3$ for the flexural strength test. These dimensions, while effective for our experimental objectives, do not strictly conform to standard sizes for earthen materials. Twenty-four hours after casting, the samples were demolded and dried for 14 days in a controlled laboratory environment maintained at a temperature of 21 °C and a relative humidity of 50%.

A 500 kN Multipurpose 500 (Controls Group) compression-flexure cement testing frame was used to determine the compressive and flexural strengths of the specimens. Two steel plates, each measuring $40 \times 40 \times 10$ mm$^3$, were employed during testing. Each specimen was centrally positioned on these plates, and the load was progressively increased at a rate of 0.5 MPa per second. The uniaxial compressive strength of the specimens was determined by the peak force recorded by the machine at the moment of specimen failure.


Figure 4: Setup of robotic cell for 3D printing of clayey soils, featuring an industrial robotic arm, mortar pump, and concrete vibrator.

### 2.9. *3D printing setup*

Figure 4 shows the robotic setup used for this research. The setup includes a KUKA KR50R2100 industrial robotic arm, capable of manipulating a payload of 50 kg over a radial range of 2100 mm. The printhead used for printing consists of a 450-mm-long metal rod mounted perpendicular to the robot flange. The 12.5-mm-diameter nozzle used in the printhead was 3D printed from PET-G. An MAI 2PUMP-PICTOR mortar pump integrating a 24 L worm pump with a flow rate of 1.5–8.5 L/min was used for the printing process. A concrete vibrator facilitated the mixture flow from the hopper to the worm pump. A GW Instek DC power supply was connected to the pump to control the flow rate by altering the voltage. A 10 m high-pressure hose delivered the mixture from the pump to the printhead mounted on top of the robotic arm.

## 3. Results and discussion

### 3.1. *Rheological properties and mix performance in green state*

#### 3.1.1. *Rheological behavior*

Figure 5 shows typical results for the rheological parameters as a function of resting time. The time scale represents the resting time (up to 45 minutes) between consecutive measurements. The cumulative time since the end of mixing is 110 minutes.

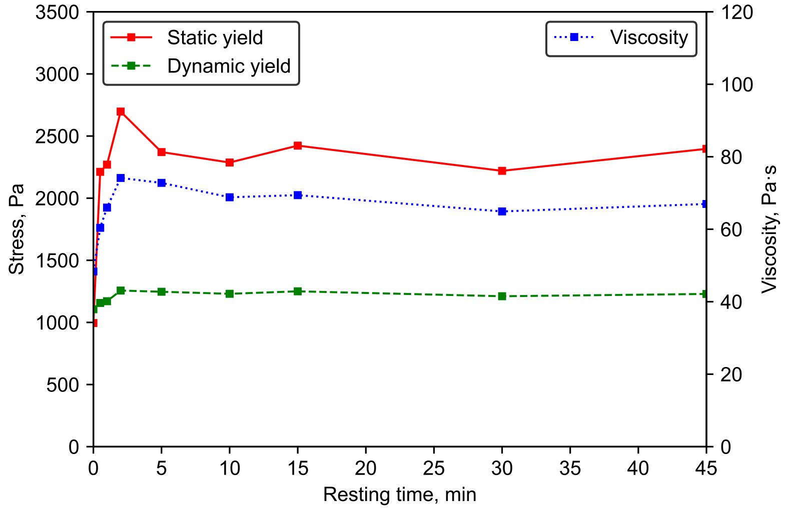


Figure 5: Rheological parameters for clayey soils as functions of resting time, showcasing the results for white kaolinite clay and sand mixtures.

In the clay-based systems studied, the static shear yield stress can be analyzed in terms of its development over two stages: re-flocculation and structuration. During re-flocculation, which occurs within the first few minutes, the increase in static shear yield stress is attributed to microstructural recovery of the platy clay particles, flocculation of the soil particles, and a change in the structure of the adsorbed water [48, 49]. Following re-flocculation, the structuration stage involves further increases in static shear stress due to material dehydration and compaction over time. The structuration of the nonstabilized clay system is not significant within the test period in this study [29].

The dynamic state of the mixture occurs when sufficient shear stress is applied to the mixture and the bonds between the particles break. The dynamic yield and apparent viscosity characterize the mixture at this stage. In the systems studied, the dynamic parameters stay stable throughout the test, as seen in Figure 5. The difference between static and dynamic shear stresses reflects the thixotropic nature of the system, which is crucial for manufacturing.

#### *3.1.2. Relations between rheological parameters and performance parameters*

We now compare the rheological characteristics of the mixtures with the actual performance parameters. Toward this end, we tested 12 clay mixtures, changing the ratio between the white-kaolinite clay and sand, as well as the water content, over a wide range (see Table 2). The composition of the mixture was characterized by a variety of tests: rheological tests, which provide the fundamental physical parameters; performance tests, including flow table tests; flow-rate tests through the printing nozzle; and the test presented in Figure 3 to determine the rigidity of the material. Figure 6 describes the correlations between the composition, rheological characteristics, and performance parameters.

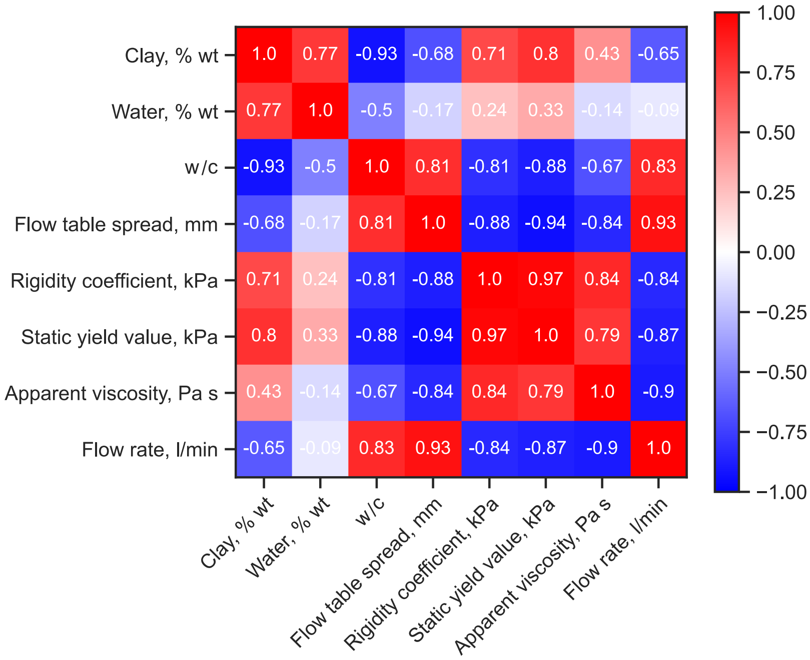


Figure 6: Statistical analysis of performance parameters in clay mixtures of varying composition, encompassing a range of water/clay and sand/clay ratios and clay content.

The flow rate correlates significantly with the apparent viscosity (−0.9) and the flow rate and static yield (−0.87), as shown in Figure 7. The strong negative correlation between the viscosity, static yield, and flow rate is typical of materials described by the Bingham model [25, 22]. This relationship emphasizes the critical role that viscosity plays in determining the effectiveness of material delivery during 3D printing.

The rigidity of the fresh mix was determined by increasingly loading the green material as described in Figure 3. The loading test was done manually and lasted about 10 minutes. Given the loading regime of the viscoelastic material, the rigidity coefficient may be considered as an

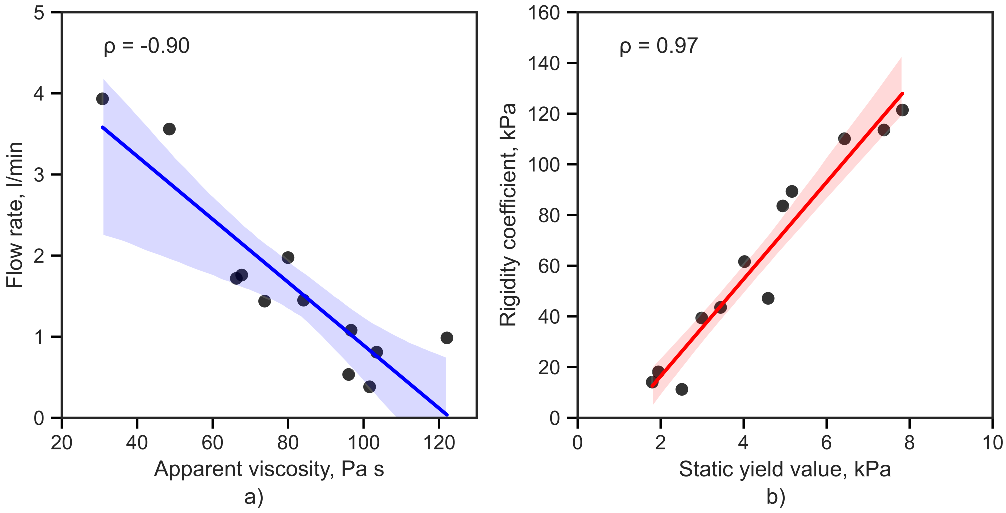


Figure 7: Statistically significant relations between basic rheological and engineering parameters: (a) relation between flow rate through the printing nozzle head and the apparent coefficient of viscosity for clay systems, and (b) relation between the rigidity of the green material and the static shear yield strength. The highlighted area represents a 95% confidence interval for this relation.

effective modulus of the mixture since the deformations registered are both elastic and plastic. The values measured in this test ranged from 10 to 120 kPa, which is consistent with previous findings for 3D printing of clayey soils [29]. The strongest correlation occurs between the rigidity coefficient and the static yield (0.97), as shown in Figure 7. This correlation is attributed to the nature of the test, which was incremental and load dependent and therefore strongly influenced by the static yield of the material. A controlled deformation test can also be used for a more precise analysis of the viscoelastic properties of such a mixture [50, 51].

### *3.1.3. Relations between performance indicators and testing methods*

The use of clayey soils in 3D printing mixtures often calls for quick, cost-effective on-site assessments. The statistical analysis, depicted in Figure 8, reveals a strong linear correlation between the flow table spread and (i) the material rigidity coefficient (−0.88) and (ii) the flow rate in the pump (0.93). This evidence suggests that the flow table test is a reliable and practical method for assessing the material flow rate through the nozzle and the material rigidity on sit.

As previously discussed, the flow rate, which is determined by the dynamic rheological parameters, is a crucial factor in 3D printing. Conversely, material rigidity is essential to ensure that the printed layers retain their intended shape. Therefore, the ability to quickly and efficiently evaluate these characteristics on-site can significantly improve the efficacy and quality of the 3D printing process.

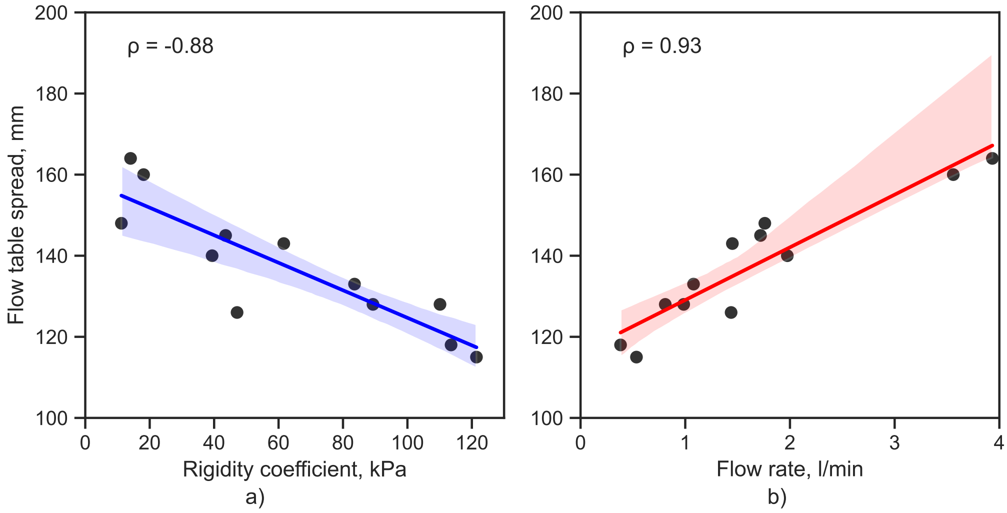


Figure 8: Statistically significant relations between performance indicators and mix composition: (a) Flow table spread as a function of rigidity coefficient and (b) of flow rate through the nozzle. The highlighted areas represent the 95% confidence interval.

### *3.1.4. Relations between performance indicators and mixture composition*

Figure 9 shows how mixture composition affects material performance. The findings reveal a moderate positive correlation between the clay/water ratio and the pump flow rate (0.83). As expected, increasing water content reduces friction between particles, which improves flow. The relationship between the clay weight percentage and the flow rate is less pronounced (−0.65), suggesting that water content is the more influential factor in this process.

Unlike traditional earth-construction methods, where optimal moisture content is typically determined based on maximum dry density [43, 52, 53], the moisture content in 3D printing should be evaluated with respect to process performance to balance flow properties and material rigidity. Furthermore, the rigidity of the mixture has a moderate negative correlation with the clay/water ratio (−0.81). In this instance, increasing water content decreases particle friction, thus reducing material rigidity. Conversely, a mild positive correlation occurs between the clay weight percentage and rigidity (0.71).

These results underscore the intricate dynamics between the components of the mixture. Therefore, the optimal balance for 3D printing mixtures likely depends on carefully tuning these ratios to accommodate both process requirements and the desired material properties.

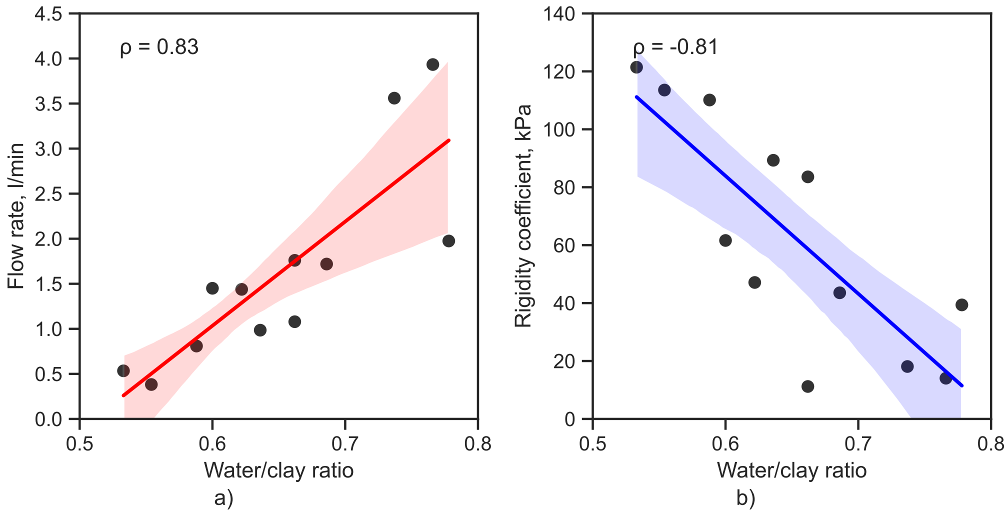


Figure 9: Statistically significant relations between performance indicators and mix composition: (a) flow rate through the nozzle as a function of water/clay ratio and (b) apparent modulus as a function of water/clay ratio. The highlighted areas represent a 95% confidence interval.

## *3.2. Design principles*

### *3.2.1. Design principles of the clayey soil mix*

The statistical analysis of relationships between rheological and performance parameters, as presented in Section 3.1, can serve as a foundation for insights that can be used to optimize the mixture of clayey soils for 3D printing applications. The analysis above implies that the overall performance of the mixture can be assessed by simultaneously considering two performance tests: the flow table test, which indicates the flow through the pumping system, and the rigidity test, which offers insight into the stability of printed layers in the green state.

Figure 10 illustrates the relationships between these two parameters for the clay systems studied here, highlighting the systems that perform adequately for 3D printing. The figure also indicates an optimal performance window, that is, the parameters of a mixture that provide a suitable combination of flow and rigidity to facilitate optimal early-age behavior, enabling both pumping and stability in the buildup of printed layers. The various tested mixtures were characterized based on their visual appearance, the results of the green method tests, and their ability to be pumped through the delivery system and characterized as either good, dry, or unstable. This approach to identifying a performance window based on relatively simple laboratory performance tests can be highly practical as a guideline for developing optimal mixtures. However, such a window serves as a ”fingerprint” that is specific to a particular printing technology. Factors such as printing system (e.g., pumping system, printing head, and nozzle) and element size and quality can affect the given window. Consequently, for different printing technologies and elements, a specific “window” must be identified.

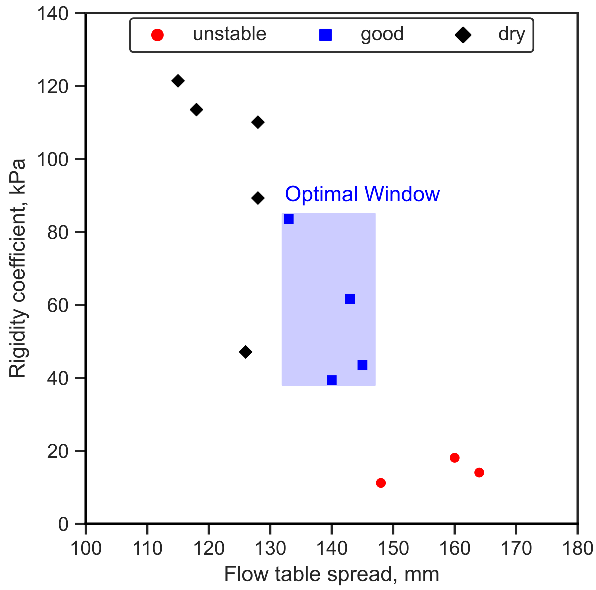


Figure 10: Rigidity coefficient plotted as a function of flow table spread, representing different compositions of the mixed-clay system (white clay/kaolinite-sand-water) and identifying a “window” of adequate overall performance for 3D printing.

#### *3.2.2. Effect of particle grading*

The mixture with a clay content of 28.6%, which resides within the “optimal window” in Figure 10, appears to produce optimal grading. This blend, with a water/clay ratio of 0.66, produces the

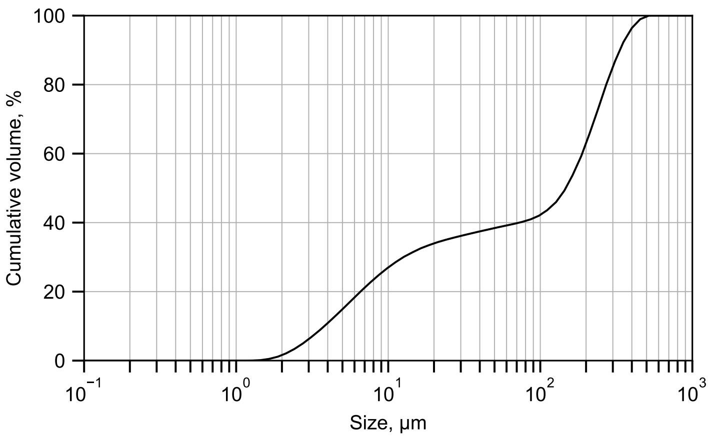


Figure 11: Grading curve representing the optimal composition of the white clay-sand mixture, yielding the best balance between flow and rigidity.

most favorable outcomes for pump flow while simultaneously ensuring satisfactory stability. Figure 11 shows the particle grading of this mixture, which underscores the role that grading plays in influencing a mixture's performance in 3D printing applications. Clay particles enhance the flow within the pumping system by forming a lubricating layer. This layer results from migration of the clay-water paste in response to inhomogeneous shear stresses present in the pipe, leading to less pressure loss during the delivery stage [54]. However, an overabundance of clay particles can inadvertently increase the viscosity of the mixture, thereby negatively impacting the flow rate through the pump [55]. Conversely, the presence of coarse granules in the mix crucially enhances the mixture's rigidity by increasing interparticle friction [56]. Therefore, designing an optimal mixture for 3D printing of soils necessitates balancing these components. The best mixture should harmoniously integrate the benefits of both clay and coarse particles, achieving a balance that optimizes both flow and stability for successful 3D printing.

### *3.2.3. In situ stability in the green state*

While the stability of deposited layers is commonly associated with their rigidity, a more comprehensive design methodology should be developed to ensure *in situ* layer stability. With this goal in mind, we applied an analytical model proposed by Kruger et al. for cement-based materials [31]. The use of this model, anchored on the analysis of the rheometer test, facilitates a better understanding of layer stability, which improves the design strategy. The shear stress at the bottom layer can be calculated as follows [31]:

$$\tau = \frac{\rho g h}{2F_{AR}}, \tag{4}$$

where $\tau$ is the shear stress (Pa), $g$ is the gravitational acceleration (m/s$^2$), $h$ is the element height (m), and $F_{AR}$ is a strength correction factor that accounts for confinement due to the layer aspect ratio ($h/w$).

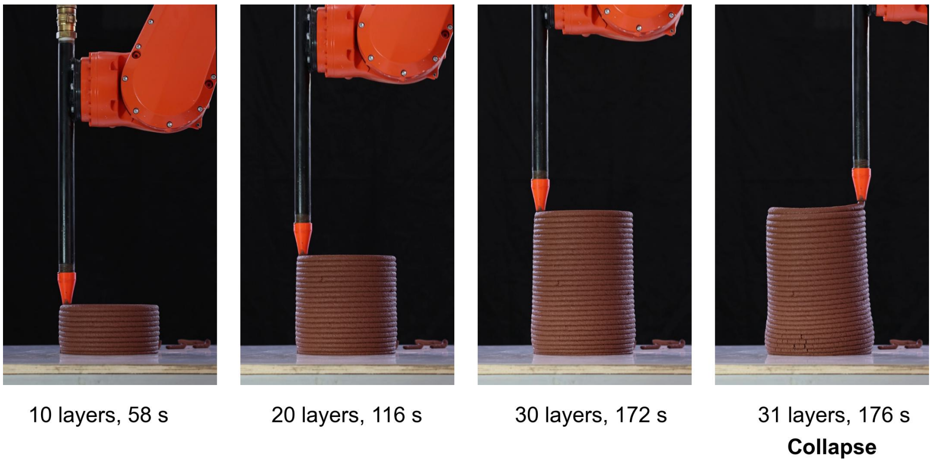


Figure 12: Printing 180-mm-diameter cylindrical column of chocolate clay mixture until collapse. Left to right: 10-, 20-, and 30-layer-high cylinder and during collapse.

To determine the point at which the bottom layer yields to the weight of the overlying layers, controlled experiments were conducted in which a cylinder was printed until collapse (Figure 12). We examined three mixtures involving white, chocolate, and Mamshit clays. The three mixtures were prepared using the optimal mixture outlined in Section 3.2. Each mixture contained a 2 : 5 clay/sand wt.% ratio. The clay/water ratio differed for each mix and was adjusted to achieve a spread of 140–145 mm in the flow table test after 25 jolts, as detailed in Table 3. A rheometer test (as described in Section 2) was conducted on each mixture after preparation, and Figure 13 shows the results. The printing test was repeated three times for each mix. Table 4 lists the parameters used for cylinder printing.

Consequently, based on equation 4 and under the specified conditions, the rate of buildup of shear stress on the lower layer of the printed cylinder is 730 Pa/min. The intersection of the shear

Table 3: Composition of white, chocolate, and Mamshit clay-sand mixtures used in tests.

| **Mix** | **Clay (wt.%)** | **Sand (wt.%)** | **Water (wt.%)** |
|---|---|---|---|
| White | 24.8 | 62.0 | 13.2 |
| Chocolate | 25.1 | 62.9 | 12.0 |
| Mamshit | 23.8 | 59.6 | 16.4 |

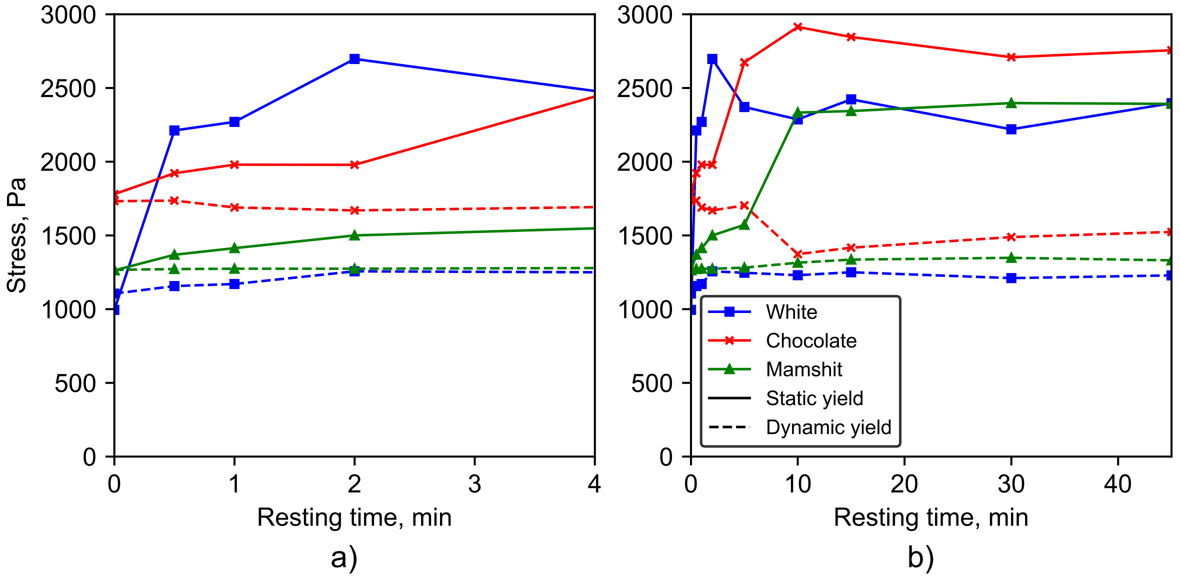


Figure 13: Influence of clay type on the rheological behavior of clay-sand mixtures (28.6% clay content): (a) 0–4 minutes resting time, (b) 0–45 minutes resting time.

stress buildup rate plotted against the static yield of the tested material, as recorded by the rheometer test, can be used to predict cylinder collapse. For example, a cylinder printed with the chocolate clay mixture under the described conditions is calculated to collapse at 3.04 minutes (184 s).

The chocolate clay mixture failed on average at 2.92 minutes, with a 6.8% coefficient of variation and an average number of layers at failure of 32. The deviation between the predicted and measured values was 4.1%, suggesting a good fit with the analytical model 14. This is consistent with failure predictions of cement-based materials [31]. In all experiments, failure is consistently due to the plastic collapse of the bottom layer [57]. Interestingly, an elastic buckling deformation occurred while printing the cylinder, which could potentially have distorted the overall shape of

Table 4: Parameters for cylinder printing.

| **Diameter (mm)** | **Nozzle velocity (mm/s)** | **Layer height (mm)** | **Layer width (mm)** | **Aspect ratio** | **Strength correction factor** | **Shear stress buildup (Pa/min)** |
|---|---|---|---|---|---|---|
| 180 | 100 | 10 | 20 | 0.5 | 1.4 | 730 |

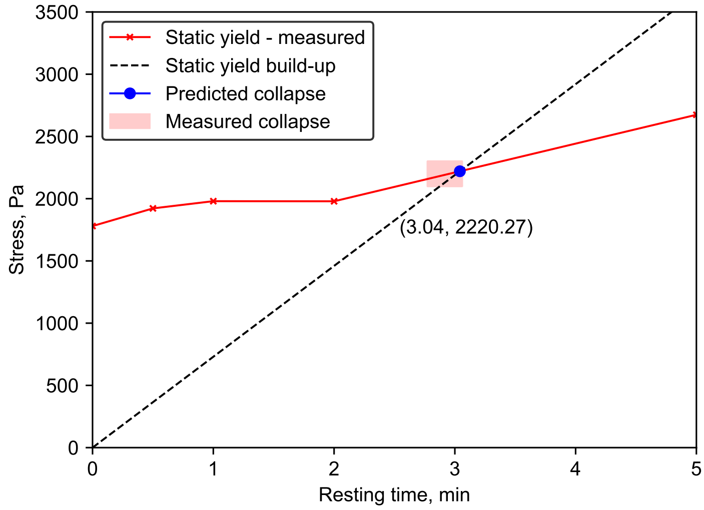


Figure 14: Intersection of calculated shear stress buildup at the bottom layer and characteristic shear yield strength for chocolate clay mixture, depicted for a 180-mm-diameter cylindrical column.

the element (as illustrated in Figure 12).

To delve deeper into the failure mechanism and ascertain the critical strain of the four lowermost layers, we applied a digital image correlation analysis (see Figure 15). The analysis reveals a 100–180 s window of the printing process, as depicted in Figure 16. The data reveal a direct correlation between the increasing dead weight on a layer and its deformation, with the greatest deformations occurring in the lowest layer. This result supports the assertion that the cylinder's failure is triggered by the yield of the lower layer upon surpassing a critical strain threshold.

Furthermore, the analysis discerns two distinct regimes during printing. The first regime is characterized by elastic behavior as evinced by a relatively linear slope of the strain that persists

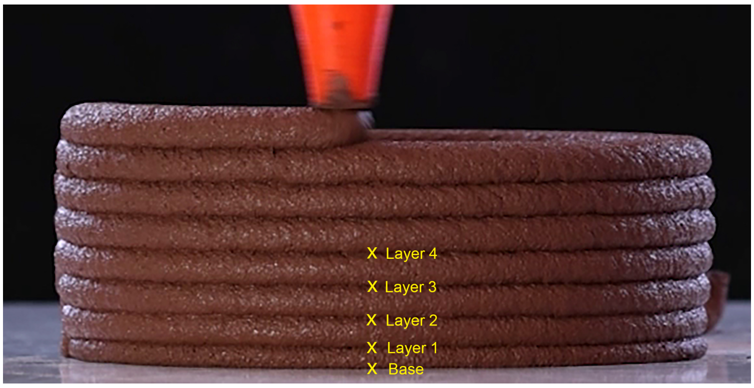


Figure 15: Digital image correlation analysis based on layer strain during 3D printing.

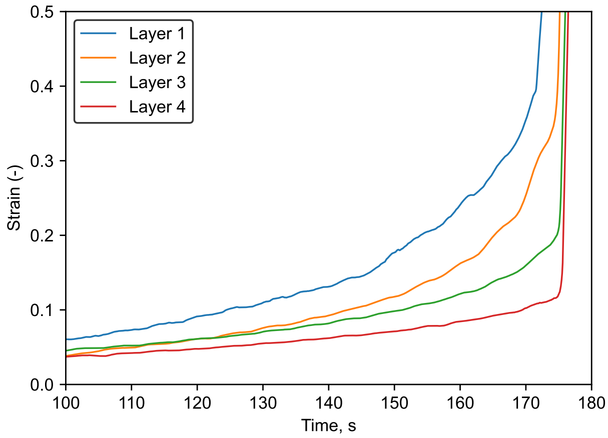


Figure 16: Lower layer strain for Chocolate clay mixture during printing of 180-mm-diameter cylinder until collapse.

until the strain reaches approximately 0.15 for the lowermost layer, or 140 s. The second regime is characterized by plastic deformation and is evinced by an exponential rise in strain up to total collapse.

The outcomes of this test demonstrate that the proposed approach leads to a sound estimate of the mechanical dynamics that occur during printing. Thus, this approach may form the foundation for developing a method to comprehensively design the entire printing operation. For example, given a specific material and design, adjusting the nozzle speed could enhance the element's stability by providing more time for the mixture to consolidate [6]. Alternatively, the mixture could be modified to better suit the buildup of static yield in the element. This could be achieved by treating the soil with various stabilizers [29, 41, 35], thereby tailoring the mixture's properties to the demands of the process.

### 3.2.4. *Effect of clay composition on stability in green state*

The three clays examined in this study vary in their mineralogical composition, particularly in terms of kaolinite content: 99.3%, 76.8%, and 41.5% for the white, chocolate, and Mamshit clays, respectively, as detailed in Table 1.

The static yield is similar for all three clay types, as shown in Figure 13. Only the chocolate clay mixture exhibits slightly higher static yields, which may be attributed to its coarser particles and wider particle-size distribution (see Figure 17) that should facilitate denser packing. Additionally, the chocolate clay mixture contains a greater fraction of silt-sized particles, which may increase the interparticle friction and, consequently, the static yield of the mixture. However, the buildup of the static yield differs considerably between the clays: it is quickest for the white clay and slowest for the Mamshit clay [see Figure 13(a): buildup time is 2, 5, and 10 minutes for the white, chocolate, and Mamshit clay, respectively]. This could be correlated with the kaolinite content in the given clay. The charged, plate-shaped particles of kaolinite form a card-house structure that increases the thixotropic effect of the mixture [58]. The individual kaolinite particles, with their layered structure and net negative charge, can experience strong electrostatic interactions with the surrounding particles and water molecules, which contributes to the formation of a stable, gel-like network in the mixture, thereby augmenting its thixotropic characteristic [59]. Furthermore, the size and shape of kaolinite particles also promote thixotropy. The thin, platy morphology of kaolinite particles leads to high specific surface area and facilitates the formation of a coherent closely knit microstructure in the mixture [60] that enhances resistance against deformation, thereby contributing to the rapid buildup of static yield stress.

To assess how clay composition and grading affect the 3D printing performance of the artifact, *in situ* stability tests were conducted on each mixture using the cylindrical-column printing method. Figure 18 shows the evolution of static yield and the intersection with shear stress buildup. Figure 19 shows photographs taken to monitor the printing process up to column collapse.

The static yield of the mixtures begins to differ in the initial minutes of the test. The Mamshit clay mix, which contains the largest volume of clay-sized particles, collapses the quickest (2.5

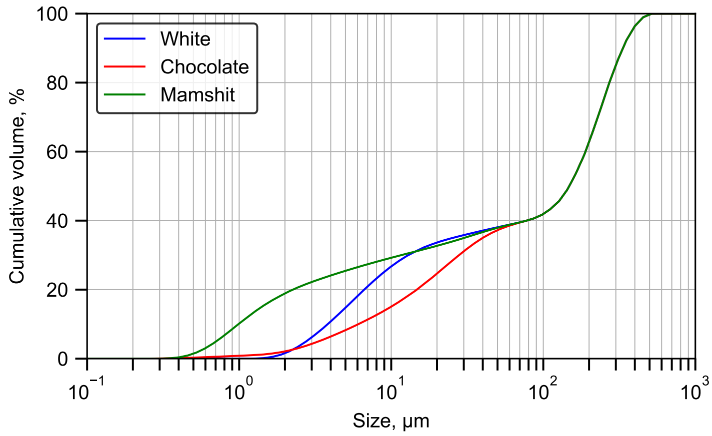


Figure 17: Particle-size distribution of the tested clay-sand mixtures.

minutes on average, 4.2% variation, 21% deviation from the analytical model). The chocolate clay mixture collapses within 2.9 minutes (5.1% variation, 4.1% deviation), and the white clay mixture collapses after 3.2 minutes (6.8% variation, 7.7% deviation).

The results show that the analytical model is consistent with the trends of the rheological test and accurately predicts the collapse time of the cylinder for the various soils tested. The pronounced deviation of the Mamshit clay mixture from the analytical model may be attributed to sensitivities connected to the procedure of the rheological test. This discrepancy can be addressed by refining the procedure of the rheological test and by allowing the mixture to homogenize over several days prior to conducting the tests. This approach should ensure a more consistent mixture and, concomitantly, more accurate predictions.

#### *3.2.5. Effect of clay composition on mechanical properties*

Figure 20 shows the results of mechanical characterization of the various soils tested. In contrast with stability in the green state, the highest compressive strength is provided by the Mamshit clay mixture, followed by the chocolate clay mixture, with the white mixture providing the least compressive strength. The results of the flexural test are similar for both the Mamshit and chocolate clay mixtures but notably lower for the white clay mixture.

The results of the compressive strength tests suggest an absence of direct correlation between the kaolinite content and the strength of the mixture, unlike the relation between kaolinite content

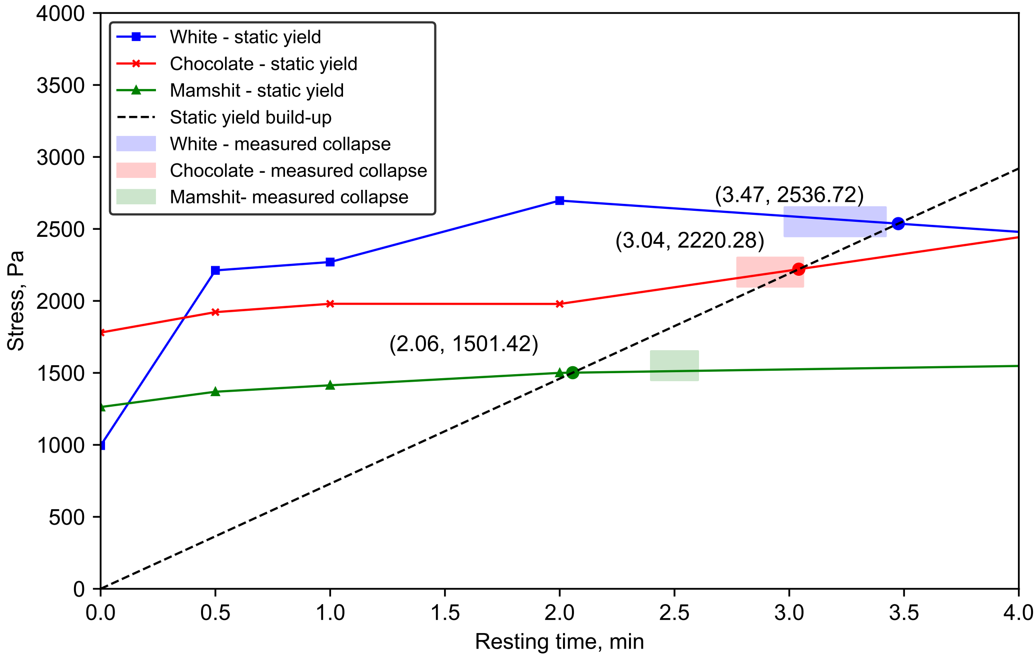


Figure 18: Calculated shear stress buildup compared with characteristic shear yield strength for three different clay mixtures in a 180-mm-diameter cylindrical column. The values calculated based on the intersection point of the two curves are shown. The highlighted rectangles indicate the range of measured collapse times.

and the rate of static yield buildup. However, the particle grading appears to significantly affect the strength of the mixture, which is consistent with the results of Cuccurullo et al. [61]. The Mamshit clay mixture, which contains a larger fraction of clay-sized particles than clay-mineral particles, is likely to prompt a denser microstructural arrangement of its constituent granules, thereby resulting in a more structurally robust mixture. The chocolate clay mixture is characterized by a coarser particle grading, which could enhance friction between particles, thus yielding positive results.

The results of mechanical characterization suggest a contradiction between the properties of the green state and those of the hardened state when optimizing clay-based mixtures for 3D printing. Although some mixtures may exhibit enhanced properties in the green state, such as an increased rate of static yield buildup, these properties may not necessarily correspond to improved mechanical properties. Nevertheless, strategies for soil stabilization might provoke a synergistic effect capable of improving the properties of both the green state and the hardened state.

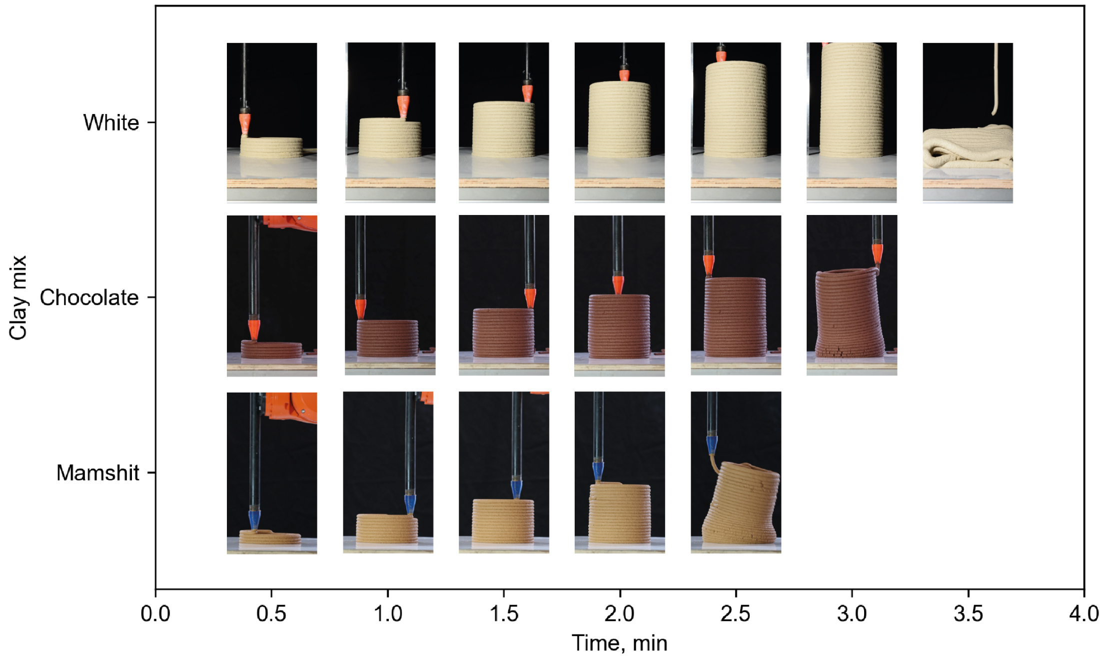


Figure 19: *In situ* stability test via cylindrical-column printing of the three clay-sand mixtures. The printing process is described in 30 s intervals until collapse.

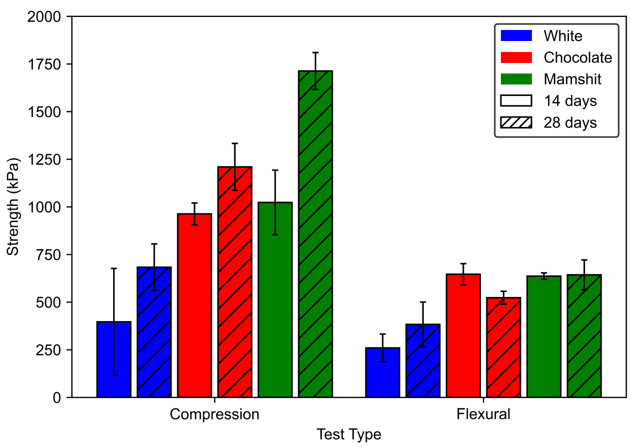


Figure 20: Compressive and flexural strengths of the mixtures tested at 14 and 28 days.

## 4. Conclusions

This study offers valuable guidelines for designing mixtures for 3D printing of clay-based soils used in construction and architecture.

Performance and rheological tests were conducted using various clay/sand and clay/water ratios.

The results of these tests revealed significant linear correlations, highlighting essential performance metrics for evaluating the mixtures. The analysis identified a robust linear relationship between rigidity and static yield stress and between flow table spread and flow rate through the pump. These findings suggest that a simple flow table test combined with a customized rigidity test provides a sufficient and cost-effective method for evaluating soil-based materials for 3D printing.

The basic rheological parameters were verified by using an analytical model to predict the stability of the green state during 3D printing. This was achieved by 3D printing a cylinder model at a constant printing rate until collapse. Bottom-layer yield caused plastic collapse for all mixtures. The *in situ* stability test provides a practical framework for fine-tuning printing parameters and layer geometry to avoid plastic collapse. The results of this test suggest that the printing parameters should be adapted according to the rheological properties of the material and the printed artifact scale. Additionally, the *in situ* test is implemented by a digital image correlation analysis, revealing that critical strain in the bottom layer is the driving force causing the collapse of the printed cylinder.

Finally, the results of this study highlight how particle-size distribution and clay mineralogy affect material performance in 3D printing. The results indicate that an increased kaolinite mineral content triggers a more pronounced thixotropic effect at the re-flocculation stage, accelerating the evolution of the static yield and thereby delaying the collapse of the structure. Furthermore, a coarser particle-size distribution enhances the static yield of the mixture.

Future work in this area should focus on better understanding and improving the thixotropy of the mixtures to optimize the design of soil-based materials for 3D printing. Such studies could refine the material's short-term thixotropy by using stabilizing agents, which would otherwise be limited and which would increase the construction rate. These modifications, however, should maintain low dynamic rheology (specifically the dynamic yield and viscosity) to ensure a smooth pumping stage. Furthermore, a microstructural investigation into how both the short- and long-term rheological properties of the mixture depend on the soil mineralogy and particle grading could provide insights allowing the optimization of design strategies of soil-based materials for 3D printing. Additionally, methods for optimizing these short-term rheological properties must go hand in hand with enhancing the material's long-term attributes, such as compressive strength, flexural strength, and durability. As these efforts progress, the environmental impact of any mineral or bio-based additives must be considered to ensure that the soil remains a low-impact and recyclable material.

## 5. Data Availability Statement

Some or all data that support the findings of this study are available from the corresponding author upon reasonable request.

## 6. Acknowledgments

The authors gratefully acknowledge the generous funding provided by the Israel Ministry of Housing and Construction under Grant No. 2031203. This financial support has been instrumental in enabling this research.

Additionally, this research benefited immensely from the support of the staff of the National Building Research Institute (Israel). Their dedication and cooperation are greatly acknowledged. Finally, we express our sincere gratitude to Research Assistant Tair Shekel for her assistance in preparing some of the illustrations presented in this paper.

## References

[1] K. L. Bar-Sinai, T. Shaked, A. Sprecher, Robotic tools, native matter: workflow and methods for geomaterial reconstitution using additive manufacturing, Architectural Science Review 64 (6) (2021) 490–503.

[2] A. Veliz Reyes, W. Jabi, M. Gomaa, A. Chatzivasileiadi, L. Ahmad, N. M. Wardhana, Negotiated matter: a robotic exploration of craft-driven innovation, Architectural Science Review 62 (5) (2019) 398–408.

[3] J.-B. Izard, A. Dubor, P.-E. Hervé, E. Cabay, D. Culla, M. Rodriguez, M. Barrado, Large-scale 3d printing with cable-driven parallel robots, Construction Robotics 1 (2017) 69–76.

[4] M. Gomaa, W. Jabi, A. V. Reyes, V. Soebarto, 3d printing system for earth-based construction: Case study of cob, Automation in Construction 124 (2021) 103577. doi:10.1016/J.AUTCON.2021.103577.

[5] G. Vantyghem, W. De Corte, E. Shakour, O. Amir, 3d printing of a post-tensioned concrete girder designed by topology optimization, Automation in Construction 112 (2020) 103084.

[6] M. Mogra, O. Asaf, A. Sprecher, O. Amir, Design optimization of 3d printed concrete elements considering buildability, Engineering Structures 294 (2023) 116735.

[7] I. Agustí-Juan, G. Habert, Environmental design guidelines for digital fabrication, Journal of cleaner production 142 (2017) 2780–2791.

[8] J.-C. Morel, A. Mesbah, M. Oggero, P. Walker, Building houses with local materials: means to drastically reduce the environmental impact of construction, Building and environment 36 (10) (2001) 1119–1126.

[9] A. Shukla, G. Tiwari, M. Sodha, Embodied energy analysis of adobe house, Renewable Energy 34 (3) (2009) 755–761.

[10] J.-C. Morel, R. Charef, E. Hamard, A. Fabbri, C. Beckett, Q.-B. Bui, Earth as construction material in the circular economy context: practitioner perspectives on barriers to overcome, Philosophical Transactions of the Royal Society B 376 (1834) (2021) 20200182.

[11] D. Ardant, C. Brumaud, A. Perrot, G. Habert, Robust clay binder for earth-based concrete, Cement and Concrete Research 172 (2023) 107207.

[12] O. Kontovourkis, G. Tryfonos, Robotic 3d clay printing of prefabricated non-conventional wall components based on a parametric-integrated design, Automation in Construction 110 (2020) 103005.

[13] S. Barnes, L. Kirssin, E. Needham, E. Baharlou, D. E. Carr, J. Ma, 3d printing of ecologically active soil structures, Additive Manufacturing 52 (2022) 102670. doi:10.1016/J.ADDMA.2022.102670.

[14] H. Alhumayani, M. Gomaa, V. Soebarto, W. Jabi, Environmental assessment of large-scale 3d printing in construction: A comparative study between cob and concrete, Journal of Cleaner Production 270 (2020) 122463. doi:10.1016/J.JCLEPRO.2020.122463.

[15] A. Chiusoli, 3D printed house TECLA - Eco-housing — 3D Printers — WASP — 3dwasp.com, https://www.3dwasp.com/en/3d-printed-house-tecla/, [Accessed 17-08-2023] (2021).

[16] A. Ellery, Sustainable in-situ resource utilization on the moon, Planetary and Space Science 184 (5 2020). doi:10.1016/j.pss.2020.104870.

[17] S. Pilehvar, M. Arnhof, R. Pamies, L. Valentini, A. L. Kjøniksen, Utilization of urea as an accessible superplasticizer on the moon for lunar geopolymer mixtures, Journal of Cleaner Production 247 (2 2020). doi:10.1016/j.jclepro.2019.119177.

[18] S. Qaidi, A. Yahia, B. Tayeh, H. Unis, R. Faraj, A. Mohammed, 3d printed geopolymer composites: A review, Materials Today Sustainability 20 (2022) 100240. doi:https://doi.org/10.1016/j.mtsust.2022.100240.
URL https://www.sciencedirect.com/science/article/pii/S2589234722001324

[19] M. Gomaa, W. Jabi, V. Soebarto, Y. M. Xie, Digital manufacturing for earth construction: A critical review, Journal of Cleaner Production 338 (2022) 130630. doi:10.1016/J.JCLEPRO.2022.130630.

[20] N. Labonnote, A. Rønnquist, B. Manum, P. Rüther, Additive construction: State-of-the-art, challenges and opportunities, Automation in construction 72 (2016) 347–366.

[21] M. T. Souza, I. M. Ferreira, E. G. de Moraes, L. Senff, A. P. N. de Oliveira, 3d printed concrete for large-scale buildings: An overview of rheology, printing parameters, chemical admixtures, reinforcements, and economic and environmental prospects, Journal of Building Engineering 32 (2020) 101833.

[22] V. Mechtcherine, F. P. Bos, A. Perrot, W. R. da Silva, V. N. Nerella, S. Fataei, R. J. Wolfs, M. Sonebi,

N. Roussel, Extrusion-based additive manufacturing with cement-based materials – production steps, processes, and their underlying physics: A review, Cement and Concrete Research 132 (2020) 106037. doi:10.1016/J.CEMCONRES.2020.106037.

[23] K. Kovler, N. Roussel, Properties of fresh and hardened concrete, Cement and Concrete Research 41 (7) (2011) 775–792.

[24] Y. Qian, S. Kawashima, Distinguishing dynamic and static yield stress of fresh cement mortars through thixotropy, Cement and Concrete Composites 86 (2018) 288–296.

[25] G. D. Schutter, D. Feys, Pumping of fresh concrete: Insights and challenges, RILEM Technical Letters 1 (2016) 76–80. doi:10.21809/rilemtechlett.2016.15.

[26] E. Buckingham, On plastic flow through capillary tubes, in: Proc. Am. Soc. Testing Materials, 1921, pp. 1154–1156.

[27] F. Bos, R. Wolfs, Z. Ahmed, T. Salet, Additive manufacturing of concrete in construction: potentials and challenges of 3d concrete printing, Virtual and Physical Prototyping 11 (2016) 209–225. doi:10.1080/17452759.2016.1209867.

[28] R. A. Buswell, W. R. L. de Silva, S. Z. Jones, J. Dirrenberger, 3d printing using concrete extrusion: A roadmap for research, Cement and Concrete Research 112 (2018) 37–49. doi:10.1016/J.CEMCONRES.2018.05.006.

[29] A. Perrot, D. Rangeard, E. Courteille, 3d printing of earth-based materials: Processing aspects, Construction and Building Materials 172 (2018) 670–676. doi:10.1016/j.conbuildmat.2018.04.017.

[30] N. Roussel, Rheological requirements for printable concretes, Cement and Concrete Research 112 (2018) 76–85. doi:10.1016/J.CEMCONRES.2018.04.005.

[31] J. Kruger, S. Zeranka, G. van Zijl, 3d concrete printing: A lower bound analytical model for buildability performance quantification, Automation in Construction 106 (10 2019). doi:10.1016/j.autcon.2019.102904.

[32] J. Kruger, M. Van den Heever, S. Cho, S. Zeranka, G. Van Zijl, High-performance 3d printable concrete enhanced with nanomaterials, in: Proceedings of the international conference on sustainable materials, systems and structures (SMSS 2019), Vol. 533, 2019, pp. 533–540.

[33] J. Kruger, S. Cho, S. Zeranka, C. Viljoen, G. van Zijl, 3d concrete printer parameter optimisation for high rate digital construction avoiding plastic collapse, Composites Part B: Engineering 183 (2020) 107660.

[34] A. Biggerstaff, M. Lepech, G. Fuller, D. Loftus, A shape stability model for 3d printable biopolymer-bound soil composite, Construction and Building Materials 321 (2022) 126337. doi:10.1016/J.CONBUILDMAT.2022.126337.

[35] A. Biggerstaff, G. Fuller, M. Lepech, D. Loftus, Determining the yield stress of a biopolymer-bound soil composite for extrusion-based 3d printing applications, Construction and Building Materials 305 (2021) 124730. doi:10.1016/J.CONBUILDMAT.2021.124730.

[36] A. Bajpayee, M. Farahbakhsh, U. Zakira, A. Pandey, L. A. Ennab, Z. Rybkowski, M. K. Dixit, P. A.

Schwab, N. Kalantar, B. Birgisson, S. Banerjee, In situ resource utilization and reconfiguration of soils into construction materials for the additive manufacturing of buildings, Frontiers in Materials 7 (3 2020). doi:10.3389/fmats.2020.00052.

[37] G. Silva, R. Ñañez, D. Zavaleta, V. Burgos, S. Kim, G. Ruiz, M. A. Pando, R. Aguilar, J. Nakamatsu, Eco-friendly additive construction: Analysis of the printability of earthen-based matrices stabilized with potato starch gel and sisal fibers, Construction and Building Materials 347 (2022) 128556.

[38] G. Bai, L. Wang, G. Ma, J. Sanjayan, M. Bai, 3d printing eco-friendly concrete containing under-utilised and waste solids as aggregates, Cement and Concrete Composites 120 (2021) 104037.

[39] A. Alqenaee, A. Memari, Experimental study of 3d printable cob mixtures, Construction and Building Materials 324 (2022) 126574.

[40] E. Ferretti, M. Moretti, A. Chiusoli, L. Naldoni, F. De Fabritiis, M. Visonà, Rice-husk shredding as a means of increasing the long-term mechanical properties of earthen mixtures for 3d printing, Materials 15 (3) (2022) 743.

[41] F. Faleschini, D. Trento, M. Masoomi, C. Pellegrino, M. A. Zanini, Sustainable mixes for 3d printing of earth-based constructions, Construction and Building Materials 398 (2023) 132496.

[42] P. Narloch, P. Woyciechowski, J. Kotowski, I. Gawriuczenkow, E. Wójcik, The effect of soil mineral composition on the compressive strength of cement stabilized rammed earth, materials 13 (2020). doi:10.3390/ma13020324. URL www.mdpi.com/journal/materials

[43] G. Minke, Building with Earth: Design and Technology of a Sustainable Architecture, 3rd Edition, Birkhäuser, 2012. doi:doi:10.1515/9783034608725.
URL https://doi.org/10.1515/9783034608725

[44] A. Ammari, K. Bouassria, M. Cherraj, H. Bouabid, S. Charif D'ouazzane, Combined effect of mineralogy and granular texture on the technico-economic optimum of the adobe and compressed earth blocks, Case Studies in Construction Materials 7 (2017) 240–248. doi:https://doi.org/10.1016/j.cscm.2017.08.004.
URL https://www.sciencedirect.com/science/article/pii/S2214509517300827

[45] ASTM International, ASTM C230/C230M - 20: Standard Specification for Flow Table for Use in Tests of Hydraulic Cement, Standard C230/C230M - 20, ASTM International, accessed: 2023-05-08 (2020).
URL https://www.astm.org/Standards/C230.htm

[46] A. Kazemian, X. Yuan, E. Cochran, B. Khoshnevis, Cementitious materials for construction-scale 3d printing: Laboratory testing of fresh printing mixture, Construction and Building Materials 145 (2017) 639–647. doi:10.1016/J.CONBUILDMAT.2017.04.015.

[47] J. Lee Rodgers, W. A. Nicewander, Thirteen ways to look at the correlation coefficient, The American Statistician 42 (1) (1988) 59–66.

[48] Y. Ren, S. Yang, K. H. Andersen, Q. Yang, Y. Wang, Thixotropy of soft clay: A review, Engineering Geology 287 (6 2021). doi:10.1016/j.enggeo.2021.106097.

[49] X. W. Zhang, L. W. Kong, A. W. Yang, H. M. Sayem, Thixotropic mechanism of clay: A microstructural investigation, Soils and Foundations 57 (2017) 23–35. doi:10.1016/j.sandf.2017.01.002.

[50] A. Perrot, D. Rangeard, A. Pierre, Structural built-up of cement-based materials used for 3d-printing extrusion techniques, Materials and Structures (2016) 1213–1220doi:10.1617/s11527-015-0571-0.

[51] R. Wolfs, F. Bos, T. Salet, Early age mechanical behaviour of 3d printed concrete: Numerical modelling and experimental testing, Cement and Concrete Research 106 (2018) 103–116.

[52] S. Cytryn, SOIL CONSTRUCTION, its principles and application for Housing, Vol. 5, The Weizman Science Press of Israel, 1958.

[53] M. C. J. Delgado, I. C. Guerrero, The selection of soils for unstabilised earth building: A normative review, Construction and Building Materials 21 (2007) 237–251. doi:10.1016/J.CONBUILDMAT.2005.08.006.

[54] S. D. Jo, C. K. Park, J. H. Jeong, S. H. Lee, S. H. Kwon, A computational approach to estimating a lubricating layer in concrete pumping, CMC 27 (2012) 189–210.

[55] M. Westerholm, B. Lagerblad, J. Silfwerbrand, E. Forssberg, Influence of fine aggregate characteristics on the rheological properties of mortars, Cement and Concrete Composites 30 (4) (2008) 274–282.

[56] J. Gong, X. Wang, L. Li, Z. Nie, Dem study of the effect of fines content on the small-strain stiffness of gap-graded soils, Computers and Geotechnics 112 (2019) 35–40.

[57] A. S. Suiker, R. J. Wolfs, S. M. Lucas, T. A. Salet, Elastic buckling and plastic collapse during 3d concrete printing, Cement and Concrete Research 135 (2020) 106016.

[58] V. Gupta, M. A. Hampton, J. R. Stokes, A. V. Nguyen, J. D. Miller, Particle interactions in kaolinite suspensions and corresponding aggregate structures, Journal of Colloid and Interface Science 359 (1) (2011) 95–103. doi:https://doi.org/10.1016/j.jcis.2011.03.043.
URL `https://www.sciencedirect.com/science/article/pii/S0021979711003195`

[59] R. Ran, S. Pradeep, S. K. Acharige, B. C. Blackwell, C. Kammer, D. J. Jerolmack, P. E. Arratia, Understanding the rheology of kaolinite clay suspensions using bayesian inference, Journal of Rheology 67 (2023) 241–252. doi:10.1122/8.0000556.

[60] E.-J. Teh, Y.-K. Leong, Y. Liu, A. Fourie, M. Fahey, Differences in the rheology and surface chemistry of kaolin clay slurries: The source of the variations, Chemical Engineering Science 64 (17) (2009) 3817–3825.

[61] A. Cuccurullo, D. Gallipoli, A. W. Bruno, C. Augarde, P. Hughes, C. L. Borderie, A comparative study of the effects of particle grading and compaction effort on the strength and stiffness of earth building materials at different humidity levels, Construction and Building Materials 306 (2021) 124770. doi:10.1016/J.CONBUILDMAT.2021.124770.